# Direct Numerical Simulation of the Flow through a Randomly Packed Pebble Bed

**Mustafa Alper Yildiz** – Corresponding Author
Department of Nuclear Engineering
Texas A&M University, College Station, TX, USA
may@tamu.edu

**Gerrit Botha**
Department of Nuclear Engineering
Texas A&M University, College Station, TX, USA
gerritbotha@tamu.edu

**Haomin Yuan**
Nuclear Science and Engineering Division
Argonne National Laboratory, Lemont, IL, USA
hyuan@anl.gov

**Elia Merzari**
Nuclear Science and Engineering Division
Argonne National Laboratory, Lemont, IL, USA
emerzari@anl.gov

**Richard C. Kurwitz**
Department of Nuclear Engineering
Texas A&M University, College Station, TX, USA
kurwitz@tamu.edu

**Yassin A. Hassan**
Department of Nuclear Engineering
Texas A&M University, College Station, TX, USA
y-hassan@tamu.edu

## Abstract

*The proposition for molten salt and high-temperature gas-cooled reactors has increased the focus on the dynamics and physics in randomly packed pebble beds. Research is being conducted on the validity of these designs as a possible contestant for fourth-generation nuclear power systems. A detailed understanding of the coolant flow behavior is required in order to ensure proper cooling of the reactor core during normal and accident conditions. In order to increase the understanding of the flow through these complex geometries and enhance the accuracy of lower-fidelity modeling, high-fidelity approaches such as direct numerical simulation (DNS) can be utilized.*

*Nek5000, a spectral-element computational fluid dynamics code, was used to develop DNS fluid flow data. The flow domain consisted of 147 pebbles enclosed by a bounding wall. In the work presented, the Reynolds numbers ranged from 430 to 1050 based on the pebble diameter and inlet velocity. Characteristics of the flow domain such as volume averaged porosity, axial porosity, and radial porosity were studied and compared with correlations available in the literature. Friction factors from the DNS results for all Reynolds numbers were compared with correlations in the literature. First- and second-order statistics show good agreement with available experimental data. Turbulence length scales were analyzed in the flow. Reynolds stress anisotropy was characterized by utilizing invariant analysis. Overall, the results of the analysis in the current study provide deeper understanding of the flow behavior and the effect of the wall in packed beds.*

# 1. Introduction

Randomly packed beds are widely used in many diverse engineering applications. These include chemical catalytic reactors, heat storage systems, and nuclear reactors. The pebble bed reactor (PBR) is one of the most promising concepts of the fourth generation of nuclear reactors. In the design of PBRs, pebbles are held in a vessel. Coolant in PBRs are either an inert gas (helium) or liquid (molten salt), which flows through the spaces between the fuel pebbles to carry the generated heat. Understanding the flow through randomly packed beds is critical for the design of pebble bed reactors.

Numerous studies of the flow through packed beds have been conducted both experimentally and computationally. A majority of the studies focused on the derivation of pressure drop correlations in randomly packed pebble beds. The pressure drop correlation proposed by Ergun [1] has been used widely in many engineering applications; however, it does not account for the walls of the bed containing the pebbles. Reichelt [2] and others conducted experimental studies and improved Ergun's correlation for a wider range of Reynolds number, porosity, and bed-to-pebble diameter ratios accounting for the effect of the walls of the bed on the pressure drop. The German Nuclear Safety Standards Commission (KTA) [3] and Association of German Engineers (VDI) [4] introduced correlations that have been used for estimating the pressure drop for high-temperature gas reactors. Eisfeld and Schnitzlein [5] proposed an improved version of Reichelt's correlation by analyzing experimental data available in the literature. Hassan and Kang [6] conducted experimental study for different bed-to-pebble diameter ratios; they developed a new correlation for pressure drop at high Reynolds numbers and low bed-to-pebble diameter ratios. Most recently, Nguyen et al. [7] conducted an experimental study of the cross-flow mixing in a randomly packed bed.

As an alternative to experiments, computational fluid dynamics (CFD) tools have been utilized to investigate flow characteristics and pressure drop through pebble bed geometries. Atmakidis and Kenig [8] conducted a CFD study to analyze the influence of the wall effects of the confining walls on the pressure drop through regular and irregularly packed beds in the laminar flow regime. Fick et al. [9] conducted a CFD study with a direct numerical simulation (DNS) approach at a Reynolds number of 7600 to analyze the flow through a structured pebble bed, in which they focused on the turbulence properties in the near-wall region. Das et al. [10] conducted a DNS study for the flow and heat transfer through a randomly packed bed for bed-to-diameter ratios varying from 4 to 8 and for Reynolds number ranging from 1 to 500. In their study they used discrete element method to generate a randomly packed bed. An extensive review of the state of knowledge of modeling the flow through porous medium was recently given by Wood et al. [11].

Our study aims to contribute on the growing pool of high-fidelity data for randomly packed pebble bed geometries. We present an analysis of the flow through randomly packed bed replicating the experimental study of Nguyen et al [7]. Our focus is on the effect of the wall on the turbulence characteristics. We also analyze the bed porosity and pressure drop through a packed bed and compare our results with available correlations.

## 2. Experimental Facility

The test facility was a closed loop at isothermal conditions that consisted of a storage tank, a primary centrifugal pump connected to a variable frequency drive to control the flow rates, a flow meter, and packed spheres. The pebble bed test section consisted of a 457.2 mm total axial length hexagonal enclosure and a circular interior cross-section with a diameter of 139.7 mm. Pebbles in the test section with 22.2 mm diameter were randomly placed in the enclosure cylinder. The test section and the spheres were made of transparent polymethyl methacrylate (acrylic). P-cymene

was utilized as the working fluid during the experiments, which had the same refractive index of the acrylic at room temperature (20 °C). The pebbles were secured by a wire mesh at the top and bottom of the experiment to prevent access movement during operating conditions.

Experiments were conducted for three modified Reynolds numbers, which were based on the effective hydraulic diameter and interstitial velocity. Effective hydraulic diameter is estimated as

$$d_h = d_p \frac{\varepsilon_b}{1-\varepsilon_b}, \tag{1}$$

where $d_p$ is pebble diameter and $\varepsilon_b$ is bulk porosity. Modified Reynolds number is defined by

$$Re_m = \frac{\rho U_m d_h}{\mu}, \tag{2}$$

where $\rho$ is the density of the working fluid, $U_m$ is interstitial velocity, and $\mu$ is the dynamic viscosity of the working fluid. Interstitial velocity $U_m$ is defined as

$$U_m = \frac{U_g}{\varepsilon_b}, \tag{3}$$

where $U_g$ is the averaged bed velocity and defined as

$$U_g = \frac{Q}{A_{bed}}, \tag{4}$$

where $Q$ is the volumetric flow rate and $A_{bed}$ is the total cross-section area of the bed.

Time-resolved particle image velocimetry (TR-PIV) measurements were conducted to obtain velocity fields at several regions of the cross-flow plane for modified Reynolds numbers ranging from 700 to 1700. More details of the experimental facility, experimental conditions, and experimental procedures are provided by Nguyen et al. [7].

# 3. Methodology

This section presents the methodology used for the current study, including the Nek5000 code, meshing strategy of the computational domain, and validity of the mesh.

## Nek5000

Nek5000 is an open source fluid/thermal simulation code based on the spectral element method, which is a high-order weighted residual technique that combines the geometric flexibility of finite elements with the rapid convergence and tensor-product efficiencies of global spectral elements [12].

In the present study, the constant property Navier-Stokes equations were solved:

$$\rho\left(\frac{\partial\vec{u}}{\partial t}+\vec{u}\cdot\nabla\vec{u}\right)=-\nabla P+\nabla\tau+\rho\vec{g} \tag{5}$$

$$\nabla\cdot\vec{u}=0\,, \tag{6}$$

where $\tau=\mu[\nabla\vec{u}+\nabla\vec{u}^{T}]$.

Nek5000 solves the Navier-Stokes equations in dimensional form. However, it can be used in nondimensional form. To this end, the Navier-Stokes equations were nondimensionalized according to following relations:

$$x^{*}=\frac{x}{L_D} \tag{7}$$

$$u^{*}=\frac{u}{U_{inlet}} \tag{8}$$

$$t^{*}=\frac{t}{L_D/U_{inlet}} \tag{9}$$

$$p^* = \frac{p}{\rho U_{inlet}^2}\ , \tag{10}$$

where $x^*$ is the nondimensional length scale, $L_D$ is the pebble diameter, $u^*$ is the nondimensional velocity scale, $U_{inlet}$ is the inlet velocity, $t^*$ is the nondimensional time scale (convective time units - CU), and $p^*$ is the nondimensional pressure scale. Based on prior experience with other simulations, using the nondimensional form of the Navier-Stokes equations makes it easier to set physical simulation times, tolerances, and so forth.

In Nek5000, pressure is solved with the Poisson equation and velocity with the Helmholtz equation. Two main solver formulations are available in Nek5000 for the Poisson equation: $P_n$-$P_n$ or $P_n$-$P_{n-2}$. In the first method, the pressure is solved on the same grid as the velocity field. The second method solves the Poisson equation in a separate internal grid that consists of fewer grid points.

In addition to its higher-order foundation, Nek5000 has further advantages that make it suitable for large-scale simulations. To speed the time to solution, it can use the method of characteristics to relax the Courant-Friedrichs-Lewy restriction or use orthogonal projections of the solution to reduce the iteration count of the algebraic solver [13].

## Computational Domain and Mesh

The flow domain under consideration consisted of 147 randomly packed pebbles. The pebble locations were obtained from the experimental facility by using a combination of PIV and image recognition algorithms. All geometric parameters were nondimensionalized by the pebble diameter. Figure 1 shows the scanned experimental test section and the computer-aided design (CAD) model of the computational domain that is used in this study.

Nek5000 supports only hexahedral elements that are constructed mostly with a blocked mesh strategy. The high curvature of the pebbles combined with the random packing structure makes the blocked mesh technique unsuitable for this geometry, however. There was no repeatable pattern, and attempts to obtain a mesh with an adequate boundary layer thickness resulted in a mesh that was impractically fine, with over 4 million elements. Therefore, we used a tet-to-hex meshing technique that has been proven useful in previous studies [14,15]. This meshing method gives a flexibility of meshing the domain of interest with fewer tetrahedral elements, which are later converted to hexahedral elements. However, the coarse mesh that was created to represent the flow domain was not sufficient to fully cover the boundary layers of the spheres and had singularity points at the contact points of the spheres due to the packing of the spheres. To overcome this issue, we modified the generated mesh in Nek5000 by moving the boundaries of the surface elements of the spheres to the exact geometrical locations of the sphere boundaries in the CAD model. Also grid points at the contact regions of the spheres were slightly moved to overcome the issue with singularity points. Moving grid points at the singularity points showed much less impact on the overall porosity of the bed compared with changing the size of the pebbles, as done by previous researchers [8]. Figure 2 shows the planar section of the final mesh, which involves approximately 866,000 hexahedral elements. For Nth polynomial expansion, each element in Nek5000 is represented by (N+1) grid points in each direction. Therefore, the number of grid points in the fifth, seventh, and ninth polynomial expansions is approximately 187 million, 444 million, and 866 million, respectively. The boundary layer thickness of the mesh was extruded such that in the fifth polynomial expansion 99.9% of the near-wall grid points have a y+ value less than 1.

Direct numerical simulation requires solving Navier-Stokes equations, resolving all the scales of motion. Characteristic scales of the smallest turbulent motions are Kolmogorov scales. In order to capture the smallest turbulent motions, one must have the grid size in the order of the scales of the smallest turbulent motions. Kolmogorov length and time scales are given as

$$\eta \equiv \left(\frac{\nu^3}{\varepsilon}\right)^{1/4}, \tag{11}$$

$$\tau \equiv \left(\frac{\nu}{\varepsilon}\right)^{1/2}, \tag{12}$$

where $\eta$ is the Kolmogorov length scale, $\tau$ is the Kolmogorov time scale, $\nu$ is the kinematic viscosity, and $\varepsilon$ is the dissipation of turbulent kinetic energy [16]. To ensure that the mesh meets the desired resolution for DNS, we calculated the Kolmogorov length scales at the third, fifth, seventh, and ninth polynomial order for all three Reynolds numbers. Figure 3 shows the ratio of the maximum grid spacing to the Kolmogorov length scale for the entire mesh. The maximum ratio was calculated by dividing the distance between elements to the local Kolmogorov length scale at each element. Figure 3 shows that in the fifth polynomial expansion, even for the highest Reynolds number, the ratio of the maximum grid size to the Kolmogorov length scale is less than 1. Production runs and analysis were conducted in the fifth polynomial expansion.

In the present study, flow is going upwards in the positive z-direction as presented in Figure 1. Periodic boundary conditions were applied at the inlet and outlet of the domain. No-slip boundary conditions were applied at the pebble surfaces and wall surfaces.

We note that the Reynolds numbers under consideration, based on the inlet velocity and pebble diameter, are 430, 740, and 1050. To prevent the confusion between the modified Reynolds number and the Reynolds number based on the inlet velocity and pebble diameter, we call lowest Reynolds number $Re_1$, the medium Reynolds number $Re_2$, and the highest Reynolds number $Re_3$.

# 4. Analysis and Results

In this section we present results of our analysis. In the first part, effect of the meshing strategy on the overall bed porosity was analyzed. In the second part, friction factor obtained from the DNS calculations were compared with pressure drop correlations from literature. In the third part, first and second order statistics from the DNS calculations were compared with available experimental data. In the fourth part, turbulence scales were analyzed in the present flow domain. Analysis of the Reynolds stress anisotropy were presented in the fifth part. Finally, coherent structures were visualized and presented in the sixth and last part.

## Bed porosity

Bed porosity is an important parameter in analyzing the flow in pebble bed configurations because it affects the pressure drop through the packed spheres. To be able to mesh the singularity points at the region of contact, we moved the grid points near the contact regions of the spheres. In the present study, it is important to check the porosity of the packed spheres before starting our analysis of the pressure drop or other quantities of interest, in order to show the effect of the meshing strategy on the porosity of the domain. The overall porosity of the domain can be calculated as follows:

$$\varepsilon = \frac{V_{void}}{V_{total}}\,, \tag{13}$$

where $V_{void}$ is the volume of the void space between pebbles and $V_{total}$ is the total volume of the domain. Before meshing the domain, we calculated the overall porosity in the CAD model using Eq. 13, which was found to be $\varepsilon = 0.430$. After meshing the flow domain, we recalculated the overall porosity as $\varepsilon = 0.436$. Moving the grid points at the contact regions of pebbles affected

the overall porosity of the flow domain only by 1.39%, which is negligible compared with earlier studies in which researchers shrunk pebble diameters by 2% to avoid the bad elements at the contact regions [8], which would yield in overall ~6% increase in the volume of the void between pebbles.

Early researchers [17–19] proposed correlations based on experimental data to calculate the overall bed porosity based on the bed-to-pebble diameter ratio. After small modifications to the contact regions, the overall porosity of the bed was compared with the proposed correlations. The bed porosity correlation by de Klerk [17] is given as

$$\varepsilon = \varepsilon_b + 0.35e^{-0.39\frac{D_{bed}}{D_{pebble}}}. \tag{14}$$

Dixon's [18] correlation is given as

$$\varepsilon = 0.4 + \frac{0.05}{D_{bed}/D_{pebble}} + \frac{0.412}{\left(D_{bed}/D_{pebble}\right)^2}, \tag{15}$$

and Jeschar's [19] correlation is given as

$$\varepsilon = 0.375 + \frac{0.34}{D_{bed}/D_{pebble}}, \tag{16}$$

where $\varepsilon_b$ is the bed bulk porosity and $D_{bed}/D_{pebble}$ is bed-to-pebble diameter ratio. Table 1 summarizes the evaluated overall porosities from the correlations along with relative errors. All three correlations predict the bed porosity with a maximum 4% difference.

Analysis of the bed porosity was further investigated in the axial and radial directions. The axial porosity profile was calculated as the ratio of the flow area at each elevation to the total cross-section of the bed. Figure 4 shows the axial porosity profile distribution. It is important to note that the effect of the inlet to the porosity is approximately 1 pebble diameter and the effect of the outlet to the bed porosity is approximately 1.5 pebble diameter. Even though in our simulations we

applied periodic boundary conditions, which would reduce the effect of inlet and outlet regions to the overall bed porosity, in our analysis we used results at $-4 \leq {}^{Z}/_{D_{pebble}} \leq -0.75$ where the axial bed porosity fluctuates around the overall bed porosity.

The radial porosity profile has an important effect on the flow channeling. The radial porosity was analyzed by extracting cylindrical layers from the computational domain starting from the bed wall towards the center of the bed at every 0.1 pebble diameter. Cylindrical layers were extracted between $-4 \leq {}^{Z}/_{D_{pebble}} \leq -0.75$ to avoid the inlet and outlet effect on the radial porosity calculations. The local porosity at each layer was calculated by taking the ratio of the flow area to total area at every extracted cylindrical layer. Figure 5 shows the radial porosity profile from the wall to the center of the bed. The radial porosity variation of the computational domain was compared with the correlation proposed by de Klerk [17] as

$$\varepsilon(r) = \begin{cases} 2.14z^2 - 2.53z + 1, & z \leq 0.637 \\ \varepsilon_b + 0.29e^{-0.6z}\left[\cos\left(2.3\pi(z - 0.16)\right)\right] + 0.15e^{-0.9z}, & z > 0.637 \end{cases}, \qquad (17)$$

where $\varepsilon(r)$ is the radial porosity and z is a nondimensional distance from wall $z = {(R - r)}/{D_{pebble}}$. The radial porosity profile has perfect agreement with de Klerk's correlation from the wall up to $R \approx 1.25D_{pebble}$. Closer to the center of the flow domain ($R \leq 1.25D_{pebble}$), de Klerk's correlation underestimates the magnitude of the radial porosity; however, the shape of the variation has good agreement in that region. Figure 6 shows the center points of the pebbles in the domain projected on the cross-section of the bed. Even though the pebbles are randomly packed, the outermost layer of pebbles shows an ordered configuration due to the alignment against the wall. The pebbles show a random configuration in the central region of the bed. Deviation of

the radial bed porosity could be due to our slight modification of the contact regions of the pebbles, which shows a greater effect in the central region of the computational domain where most of the pebbles are located. Nonetheless, the radial bed porosity profile shows good agreement with de Klerk's correlation.

## Pressure Drop

Pressure drop is an important parameter in the design of the packed bed reactors in terms of the required energy for maintaining the flow. The friction factors found in our simulations were compared with available correlations proposed by early researchers. The best-known correlation, proposed by Ergun [1], has the following form:

$$\frac{\Delta P}{L} = A\nu U + BU^2, \tag{18}$$

where $U$ is the superficial velocity, $\nu$ is the kinematic viscosity of the working fluid, and constants A and B are determined based on the experimental data. In this correlation, the pressure drop is expressed in terms of viscous and kinetic energy losses. The first term in the right-hand side (RHS) of Eq. 18 represents the contribution of shear stresses at the wall and pebble surfaces, which are especially effective in the Darcy regime (at low Reynolds number). The second term in the RHS represents the contribution of the flow inertia to the pressure drop, which effectively brings the contribution to the pressure drop in the Forcheimer regime (high Reynolds number). Since Ergun's correlation is for an infinite packed bed, it does not account for the confining wall. In reality, however, packed beds are bounded with a confining wall, which brings additional resistance to the flow through the bed. Ergun's correlation has been improved to account for confining walls for different bed-to-pebble diameter ratios and Reynolds numbers. Some of the friction factor

correlations through packed beds [1,3–5] that were compared with results from our DNS calculations are listed in Table 2.

The pressure drop from the simulation was calculated as $-4 \leq Z/D_{pebble} \leq -0.75$ and compared with proposed correlations. Figure 7 shows the comparison of the friction factor calculated from the DNS data at three modified Reynolds numbers with the proposed empirical correlations. Ergun's correlation shows big deviations from the DNS friction factors, since it does not account for the effect of the confining walls. The friction factor calculated from the DNS data is within the error band of the Eisfeld and Schnitzlein, KTA, and VDI correlations. We note that as the Reynolds number decreases, the error between the correlations and the DNS data increases, which is in agreement with Eisfeld and Schnitzlein's [5] observations that the wall effect on the pressure drop is more important in low Reynolds number cases for $D_{bed}/D_{pebble}$ below 10.

## First- and Second-Order Statistics

Figure 8 shows the instantaneous velocity snapshot in the flow domain for the highest Reynolds number ($Re_3$). Pebbles in the outer ring (Figure 6) show an ordered structure that creates flow channels near the wall region (half a diameter from the wall). Flow channels near the wall can be clearly seen in the instantaneous velocity snapshot (Figure 8).

Figure 9 shows the normalized average velocity field at the $Z/D_{pebble} = -2.28$ cross-section along with the three selected line locations where the first- and second-order statistics from DNS data was compared with the experimental data of Nguyen et al.[7]. Line 1 extends from the bed wall to the pebble wall. Line 2 and Line 3 extend in the gaps between pebbles.

First- and second-order statistics were averaged for seventeen flow through times (85 convective units), where one flow through time is approximately 5 convective units. Figure 10 shows the time-

averaged velocity and Reynolds stress profiles on line 3 for different time window lengths. It can be seen that the velocity and Reynolds stress fields are insensitive to time window length after seventeen flow through times.

Figure 11 shows a comparison of the normalized averaged velocity components for the three lines. The average velocity profiles are plotted against the length of the sampling line. The average velocity profiles for the three selected lines show good correlation with the experimental data.

Figure 12 shows a comparison of the normalized Reynolds stress components for the selected three lines. The Reynolds stress components on the second and third lines show very good agreement with experimental data. The lowest Reynolds number ($Re_1$) on the first line shows some deviations from the experimental data; however Reynolds stresses for $Re_2$ and $Re_3$ show good agreement with experimental data.

Overall, comparison of the first and second-order statistics with the experimental data of Nguyen et al. shows good agreement.

## Integral Scales

To quantify the structures within the flow, we analyze turbulence scales with the two-point correlation analysis. To evaluate the resolved time or length scale, we can apply the two-point velocity cross-correlation,

$$R_{uu}(x_r, \eta, \tau) = \frac{\langle u'(x_r, t)u'(x_r + \eta, t + \tau)\rangle}{u'_{rms}(x_r, t)u'_{rms}(x_r + \eta, t)}, \tag{19}$$

where $u'$ is the fluctuating part of the velocity component, $x_r$ is the coordinate of the reference point, $\tau$ is the lag time, and $\eta$ is the distance between two velocity realizations. Cross-correlation between two points can be estimated by setting the lag time $\tau = 0$ and increasing the distance

between the two velocity realizations $\eta$. Autocorrelation of the signal can be estimated by setting $\eta = 0$ and changing the lag time $\tau$.

The integral length scale of a large-energy-containing eddy can be estimated by

$$L_{int} = \int_0^{\eta_s} R_{ii}(x, \eta)\, d\eta, \tag{20}$$

where $\eta_s$ is the total separation distance in space between two points where the correlation function intercepts zero.

Fluctuating velocity components were recorded along the sampling lines shown in Fig. 13. Lines L1 and L2 were located near the confining wall, where the flow channeling occurs. Lines L3–L6 are located in the central part of the bed closer to the inlet, and lines L7–L9 are in the central part of the packed bed closer to the outlet. All lines in the central part of the packed bed (L3–L9) are within $-4 \leq Z/D_{pebble} \leq -0.75$ where the bed axial porosity is not affected by the inlet or outlet region.

Cross-correlations were analyzed for all Reynolds numbers along each line. Here we present cross-correlation profiles only for the highest Reynolds number. Figure 14(a) shows the cross-correlation of the velocity fluctuations in the x-direction along lines L6 and L9. Figure 14(b) shows the cross-correlation of the velocity fluctuations in the y-direction along lines L5 and L7, and Fig. 14(c) shows the cross-correlation of the velocity fluctuations in the z-direction along lines L2, L4, and L8. A common feature of cross-correlation functions in all three directions is that the decay rate of the cross-correlation function along the lines closer to the inlet part of the flow domain is smaller than the lines that are close to the outlet region. This indicates that the big turbulent structures with low frequencies that were formed at the beginning of the bed break down into smaller eddies with higher frequencies. This process also indicates that the mixing closer to the end of the bed is higher than in the inlet region. Integral length scales in the x-direction at lines L6 and L9 were calculated

as $0.1554D_{pebble}$ and $0.0973D_{pebble}$; in the y-direction for lines L5 and L7 as $0.1284D_{pebble}$ and $0.0926D_{pebble}$; and in the z-direction for lines L2, L4, and L8 as $0.1549D_{pebble}$, $0.1402D_{pebble}$, and $0.075D_{pebble}$, respectively. In the z-direction along line L2, which is close to the bed wall, the integral length scale is higher than at the locations in the center of the bed. This shows that flow near the confining wall is less disturbed due to channeling effects.

## Reynolds Stress Anisotropy

The Navier-Stokes equation describes the interplay between the elementary flow processes due to inertia, pressure, viscous forces, and, when present, body forces. The sole action of pressure is to render the velocity field deformed by inertia and to reorient the velocity fluctuations in a manner that preserves the divergence-free condition. Correspondingly, pressure-strain redistribution redistributes kinetic energy among three diagonal Reynolds stress components. The action of pressure gradually leads to the isotropization of the fluctuations as they cascade down the scales. Invariant analysis of the Reynolds stress tensor proposed by Lumley and Newman [20] is employed to characterize turbulence and to more deeply understand the structure of the turbulent flow in packed beds.

Any symmetric second-order tensor, such as the Reynolds stress tensor $\mathcal{R}_{ij}$, can be divided into isotropic ($\mathcal{R}_{ij}^{I}$) and anisotropic ($\mathcal{R}_{ij}^{A}$) parts, where $\mathcal{R}_{ij}^{I} = \frac{1}{3}\mathcal{R}_{ij}\delta_{ij}$ and $\mathcal{R}_{ij}^{A} = \mathcal{R}_{ij} - \frac{1}{3}\mathcal{R}_{ij}\delta_{ij}$. The anisotropic part of the Reynolds stress tensor can be manipulated as follows,

$$b_{ij} = \frac{\mathcal{R}_{ij}^{A}}{\mathcal{R}_{ii}} = \frac{\mathcal{R}_{ij}}{\mathcal{R}_{ii}} - \frac{1}{3}\delta_{ij}, \tag{21}$$

where $b_{ij}$ is the nondimensional anisotropic part of the Reynolds stress tensor. For a symmetric second-order tensor, three principal invariants are defined as

$$I = b_{ii} = trace(b), \tag{22}$$

$$II = \frac{1}{2}[(b_{ii})^2 - b_{ii}^2], \tag{23}$$

$$III = det(b), \tag{24}$$

where $I$, $II$, and $III$ are the first, second, and third invariants, respectively. The first invariant of the anisotropic tensor is always zero for incompressible flow because of its normalization. Consequently, the anisotropy tensor has two independent invariants, which can be used to map the state of the Reynolds stress tensor in a turbulence triangle in invariant coordinates of the local degree of three-dimensionality ($\eta$) and the characteristic shape associated with the particular balance of stresses ($\xi$) [21,22]. The variables $\eta$ and $\xi$ are defined as

$$\xi^3 = \frac{III}{2}, \qquad \eta^2 = -\frac{II}{3}. \tag{25}$$

The overall anisotropy in the Reynolds stress tensor can be estimated by combining invariants into single function that scales anisotropy from 0 to 1 and is given by [22,23]

$$F = 1 - 27\eta^2 + 54\xi^3. \tag{26}$$

Figure 15 shows the turbulence triangle with the limits of the realizable turbulence. The gradient inside the turbulence triangle represents the overall anisotropy state in the Reynolds stress tensor. We conducted Reynolds stress anisotropy analysis near the confining wall and at the inner region of the packed bed for the highest Reynolds number of our simulations. Nine lines were selected for the analysis; the locations of the lines in the domain are shown in Figure 13. Figure 16 shows the return-to-isotropy trajectories of the selected four lines on the turbulence triangle. The evolution of the Reynolds stress invariants moving along line L1 (from the bed wall to the center of the bed) shows evolution similar to that of the channel flow up to log-law region ($y^+ \approx 32$), where farther from the wall with the effect of the flow around near-wall pebbles, the anisotropy

state returns to a one-component turbulence state and closer to the pebble wall it returns to a two-component state. Moving downstream on line L2, the state of the Reynolds stress tensor moves to the isotropic state twice, which corresponds to locations after flow passes two pebbles close to the wall. Flow passing between the wall and the pebbles generates a rod-like turbulence. As a general trend for lines in the central region of the bed (L3–L9), the state of Reynolds stress tensor shows mainly two-dimensional turbulence near the walls of the pebbles and nearly isotropic turbulence in the gap between the pebbles. In Fig. 16 we plotted state of anisotropy for L3. Lines L4-L8 were not shown in Figure 16 since they show very similar behavior to L3. Line 9 (L9) shows a different behavior at the end point, where the state of the turbulence shifts to the one-component turbulent state. Figure 13 shows that the end point of L9 is in between two pebbles, which accelerates the flow in the streamwise direction; and the pressure to keep the divergence-free condition moves energy from two other components of fluctuations to the third component, which results in the one-component turbulent state.

To have a broader view of the state of turbulence, in Fig. 17 (top) we plotted the anisotropy factor (F) on planes crossing x=0 (Fig. 17 top left) and y=0 (Fig. 16 top right). At the near-bed-wall region and around pebbles, the anisotropy factor shows low values, suggesting an anisotropic state of turbulence. Behind the pebbles at the wake region, the anisotropy factor shows higher values around F=0.7-0.8; and before and after the pebble region close to the inlet and outlet of the domain, the anisotropy factor is at around F=0.85-0.95, which indicates an isotropic state of turbulence.

The turbulent kinetic energy (TKE) is produced by the action of the mean velocity gradients working against the Reynolds stresses. This action removes the kinetic energy from the mean flow and transfers it to the fluctuating velocity field. The anisotropic part of the Reynolds stress tensor is known to affect the production of the turbulent kinetic energy, which is given by

$$\mathcal{P} = -b_{ij}\bar{S}_{ij}, \tag{27}$$

where $b_{ij}$ is the anisotropic part of the Reynolds-stress tensor given by Eq. 21 and $\bar{S}_{ij}$ is the mean rate of strain given by

$$\bar{S}_{ij} = \frac{1}{2}\left(\frac{\partial\langle U_i\rangle}{\partial x_j} + \frac{\partial\langle U_j\rangle}{\partial x_i}\right). \tag{28}$$

Figure 17 (bottom) shows the production of the turbulent kinetic energy on planes x=0 (Fig. 17 bottom left) and y=0 (Fig. 17 bottom right). One can see that the production of TKE follows the trend of the anisotropy factor closely. On both planes (x=0 and y=0), production of TKE is higher where the Reynolds stresses are more anisotropic. It is also important to notice regions of negative production in the domain. It can be seen that the negative production occurs at the regions of flow acceleration. The negative production causes local laminarization of the flow and increases isotropy. As the flow starts to decelerate production increases and increases anisotropy. This behavior is present throughout the bed as it can be seen at the zoomed-in view in Figure 17.

## Vortex Visualization

Vortex structures were visualized with the $\lambda_2$ criterion developed by Jeong and Hussain [24]. According to this method, the vortex is defined by the negative eigenvalue of $S_{ik}S_{kj} + \Omega_{ik}\Omega_{kj}$, where $S_{ij}$ and $\Omega_{ij}$ are the symmetric and antisymmetric parts of the velocity gradient tensor, respectively. Figure 18 shows the vortex structures identified near the bed wall (left) and at the center of the bed (right). Near the wall region, vortices were visualized within half a pebble diameter from the wall, where at the center of the domain vortices were visualized within one pebble diameter in the cylindrical region. In both regions, vortexes were visualized at $\lambda_2 = -300$ $CU^{-2}$. One can see that the hairpin-type coherent structures in the central region of the bed appear

denser than in the wall region, suggesting that big structures formed in the central region break down into smaller structures while moving downstream, because of their complex geometry; in contrast, near the wall, vortical structures tend to move downstream unobstructed through semi-regular channels formed by the ordered structure of the pebbles near the wall.

## 5. Conclusion

In this study, we analyzed flow through a randomly packed bed with direct numerical simulation using the spectral element code Nek5000. Kolmogorov scales were calculated to demonstrate the mesh validity for the DNS study, which showed that the developed mesh is capable of capturing the smallest scales of turbulent motion in the domain. Radial and axial porosity of the bed along with overall bed porosity was analyzed and porosity distribution was compared with available correlations. We demonstrated that the meshing strategy employed in the present study has negligible effect on bed porosity. The pressure drop through packed bed was calculated and compared with available correlations, which showed agreement within error margins of the correlations. Time-averaged first- and second-order statistics were validated with available experimental data. Results showed very good agreement for the first-order statistics and satisfactory agreement for the second-order statistics. The state of the turbulence was analyzed within packed bed spheres near the wall and inside the domain to deepen our understanding of flow physics in this type of flow. Results showed an anisotropic state of turbulence near the walls of the bed and the pebbles and a more isotropic state of turbulence at the wakes of the pebbles in the center of the domain. The production of the turbulent kinetic energy was shown to follow the isotropic state of the Reynolds stresses. Vortices near the wall region and in the central region were identified through the $\lambda_2$ criterion. Denser, smaller flow structures were observed in the central

region compared with structures in the near-wall region where larger elongated structures are observed.

## Acknowledgments

We thank Dr. Thien Nguyen for providing the experimental data, and we acknowledge the invaluable advice from peers at Texas A&M University and Argonne National Laboratory. We thank the Argonne Leadership Computing Facility (ALCF) for providing the computational resources. This material was based on work supported by the U.S. Department of Energy, Office of Science, under contract DE-AC02-06CH11357.

# References


[1] Ergun, S., 1952, “Fluid Flow through Packed Columns,” Chem. Eng. Prog., **48**(2), pp. 89–94.

[2] Reichelt, W., 1972, “Zur Berechnung Des Druckverlustes Einphasig Durchstromter Kugel-Und Zylinderschuttungen,” Chemie-Ingenieur-Technik, **44**, pp. 1068–1071.

[3] Ausschusses, K., and Postfach, S., 1981, “Nuclear Safety Standards Commission ( KTA ) Reactor Core Design of High-Temperature Gas-Cooled Reactors Part 3 : Loss of Pressure through Friction in Pebble Bed Cores,” **49**(March).

[4] Wirth, K.-E., 2010, “Pressure Drop in Fixed Beds,” *VDI Heat Atlas*, pp. 1106–1110.

[5] Eisfeld, B., and Schnitzlein, K., 2001, “The Influence of Confining Walls on the Pressure Drop in Packed Beds,” Chem. Eng. Sci., **56**(14), pp. 4321–4329.

[6] Hassan, Y. A., and Kang, C., 2012, “Pressure Drop in a Pebble Bed Reactor Under High Reynolds Number,” Nucl. Technol., **180**(2), pp. 159–173.

[7] Nguyen, T., Muyshondt, R., Hassan, Y. A., and Anand, N. K., 2019, “Experimental Investigation of Cross Flow Mixing in a Randomly Packed Bed and Streamwise Vortex Characteristics Using Particle Image Velocimetry and Proper Orthogonal Decomposition Analysis,” Phys. Fluids, **31**(2), p. 025101.

[8] Atmakidis, T., and Kenig, E. Y., 2009, “CFD-Based Analysis of the Wall Effect on the Pressure Drop in Packed Beds with Moderate Tube/Particle Diameter Ratios in the Laminar Flow Regime,” Chem. Eng. J., **155**(1–2), pp. 404–410.

[9] Fick, L., Merzari, E., and Hassan, Y., 2015, “Direct Numerical Simulation of the Flow through a Structured Pebble Bed near a Wall Boudary,” *ASME-JSME-KSME 2015 Joint*

*Fluids Engineering Conference*, Seoul, Korea.

[10] Das, S., Deen, N. G., and Kuipers, J. A. M., 2017, "A DNS Study of Flow and Heat Transfer through Slender Fixed-Bed Reactors Randomly Packed with Spherical Particles," Chem. Eng. Sci., **160**(May 2016), pp. 1–19.

[11] Wood, B. D., He, X., and Apte, S. V., 2020, "Modeling Turbulent Flows in Porous Media," Annu. Rev. Fluid Mech., **52**(1), pp. 171–203.

[12] "Nek5000 Version 17.0. Argonne National Laboratory, Illinois" [Online]. Available: http://nek5000.mcs.anl.gov.

[13] Offermans, N., Marin, O., Schanen, M., Gong, J., Fischer, P., Schlatter, P., Obabko, A., Peplinksi, A., Hutchinson, M., and Merzari, E., 2016, "On the Strong Scaling of the Spectral Element Solver Nek5000 on Petascale Systems," *EASC '16 Proceedings of the Exascale Applications and Software Conference*.

[14] Yildiz, M. A., Yuan, H., Merzari, E., and Hassan, Y. A., 2019, "Numerical Simulation of Isothermal Flow Across Slant Five-Tube Bundle with Spectral Element Method Code Nek5000," Nucl. Technol., pp. 1–11.

[15] Yildiz, M. A., Merzari, E., and Hassan, Y. A., 2019, "Spectral and Modal Analysis of the Flow in a Helical Coil Steam Generator Experiment with Large Eddy Simulation," Int. J. Heat Fluid Flow, **80**.

[16] Stephen B. Pope, 2000, *Turbulent Flows*, Cambridge University Press.

[17] De Klerk, A., 2003, "Voidage Variation in Packed Beds at Small Column to Particle Diameter Ratio," AIChE J., **49**(8), pp. 2022–2029.

[18] Dixon, A. G., 1988, "Correlations for Wall and Particle Shape Effects on Fixed Bed Bulk

Voidage," Can. J. Chem. Eng., **66**(5), pp. 705–708.

[19] Jeschar, R., 1964, "Druckverlust in Mehrkornschüttungen Aus Kugeln," Arch. für das Eisenhüttenwes., **35**(2), pp. 91–108.

[20] Lumley, J. L., and Newman, G. R., 1977, "The Return to Isotropy of Homogeneous Turbulence," J. Fluid Mech., **82**, pp. 161–178.

[21] Choi, K. S., and Lumley, J. L., 2001, "The Return to Isotropy of Homogeneous Turbulence," J. Fluid Mech., **436**, pp. 59–84.

[22] Hamilton, N., Tutkun, M., and Cal, R. B., 2017, "Anisotropic Character of Low-Order Turbulent Flow Descriptions through the Proper Orthogonal Decomposition," Phys. Rev. Fluids, **2**(1), pp. 1–33.

[23] Smalley, R., Leonardi, S., Antonia, R., Djenidi, L., and Orlandi, P., 2002, "Reynolds Stress Anisotropy of Turbulent Rough Wall Layers," Exp. Fluids, **33**(1), pp. 31–37.

[24] Jeong, J., and Hussain, F., 1995, "On the Identification of a Vortex," J. Fluid Mech., **285**, pp. 69–94.

# List of Tables

# List of Figures

Figure 18: Instantaneous isosurfaces of $\lambda_2$ near the enclosing wall (left) at the center of the bed (right).

## Figures

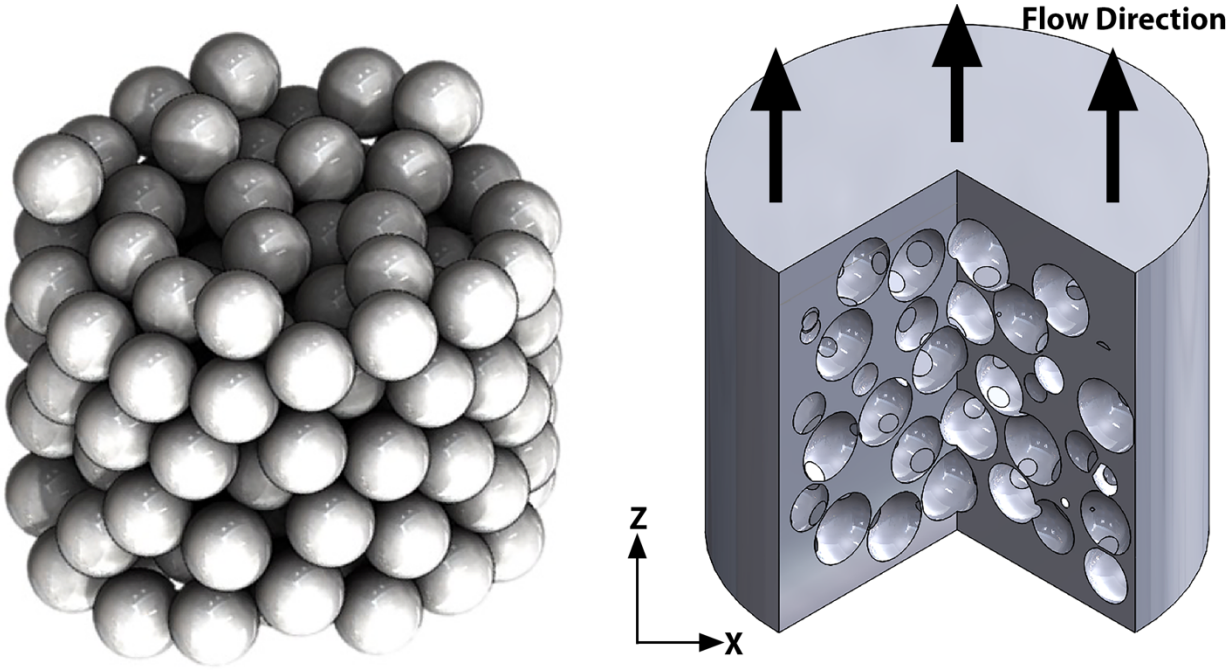


Figure 1: Visualization of scanned experimental test section (left) and CAD model of the flow domain (right)

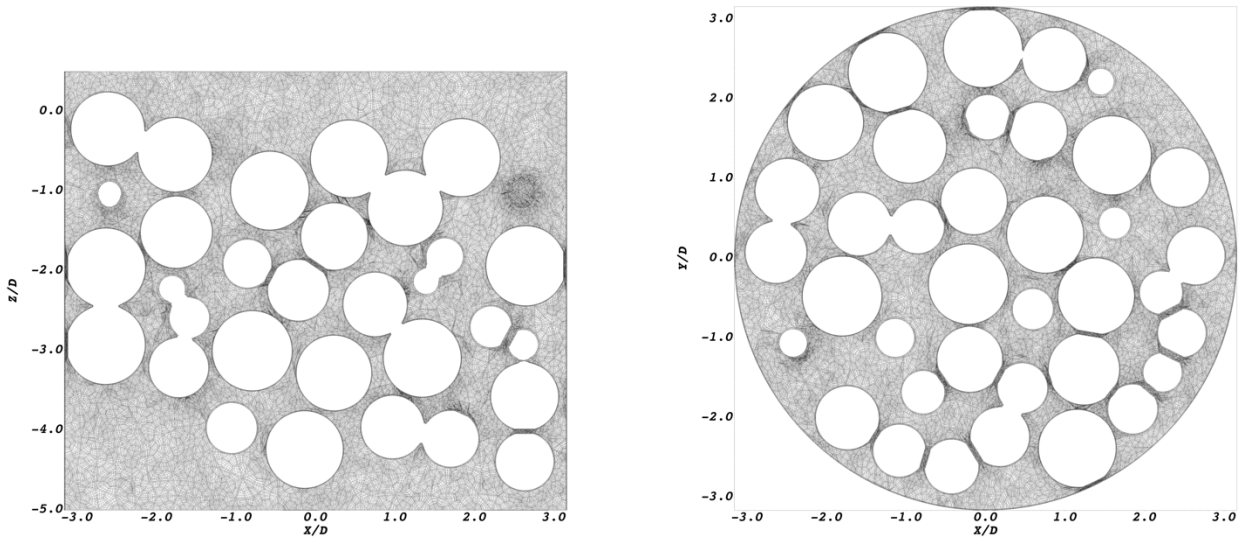


Figure 2: Planar sections of the mesh

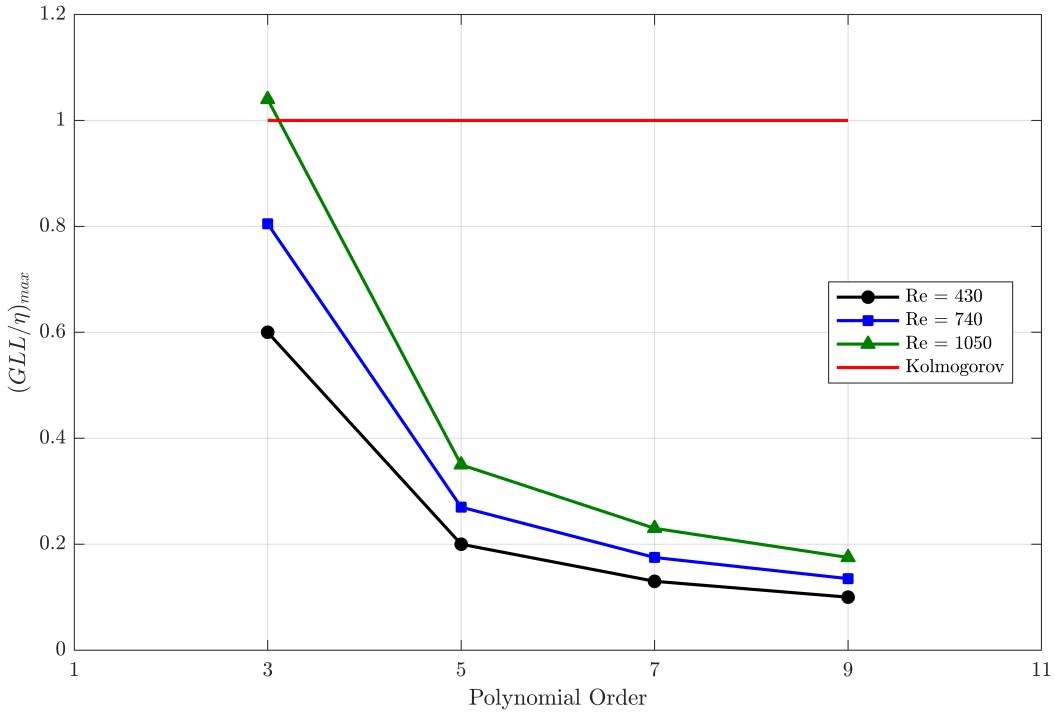


Figure 3: Ratio of the maximum grid spacing to Kolmogorov length scale

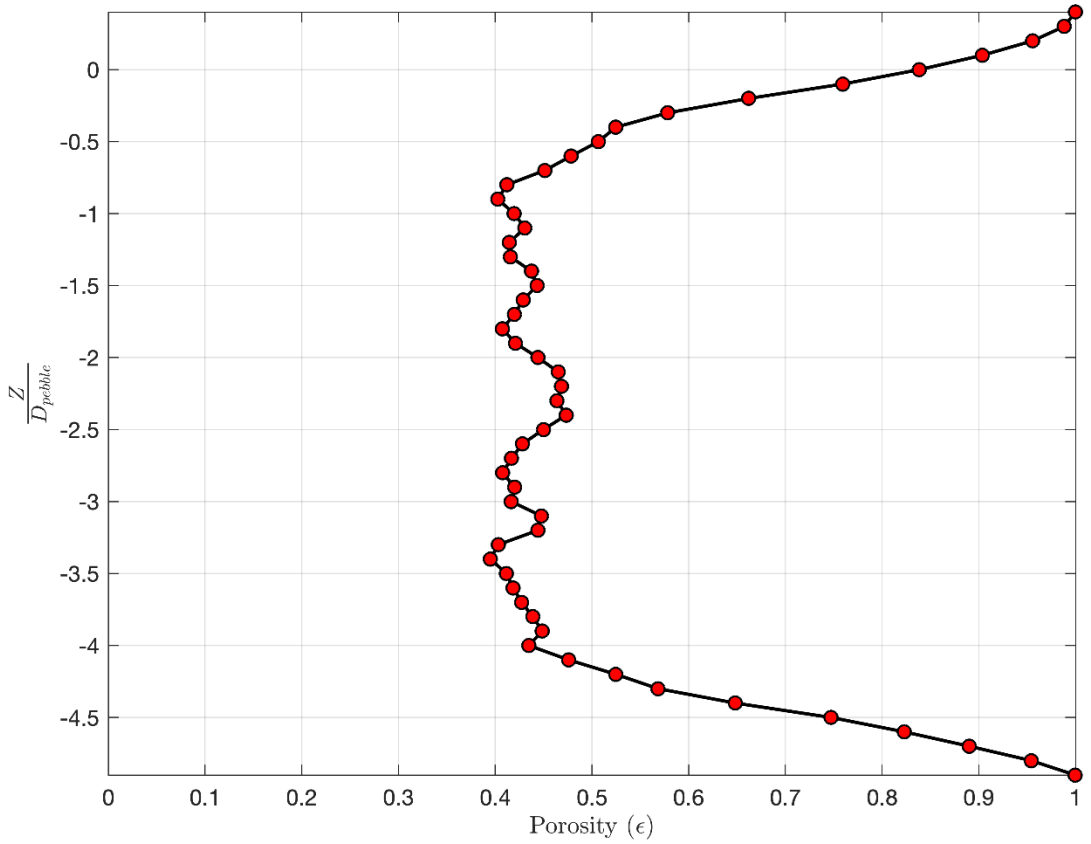


Figure 4: Axial porosity profile along the flow domain

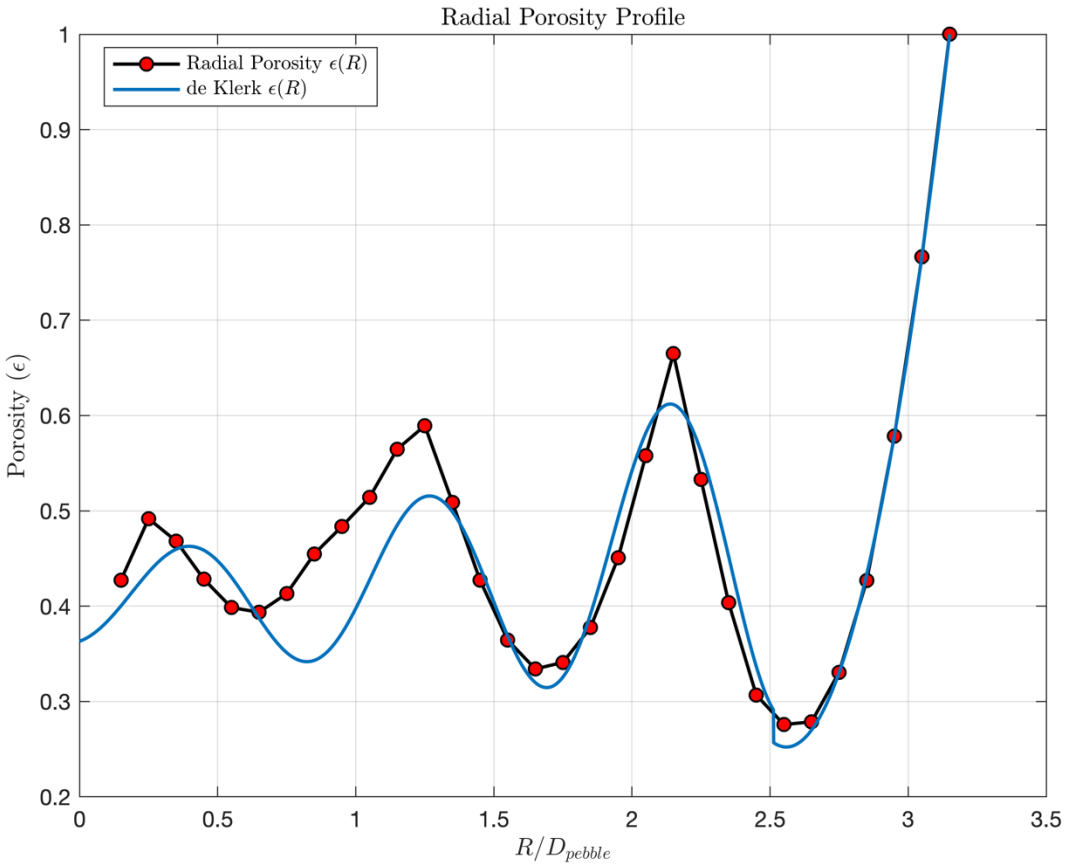


Figure 5: Radial porosity profile

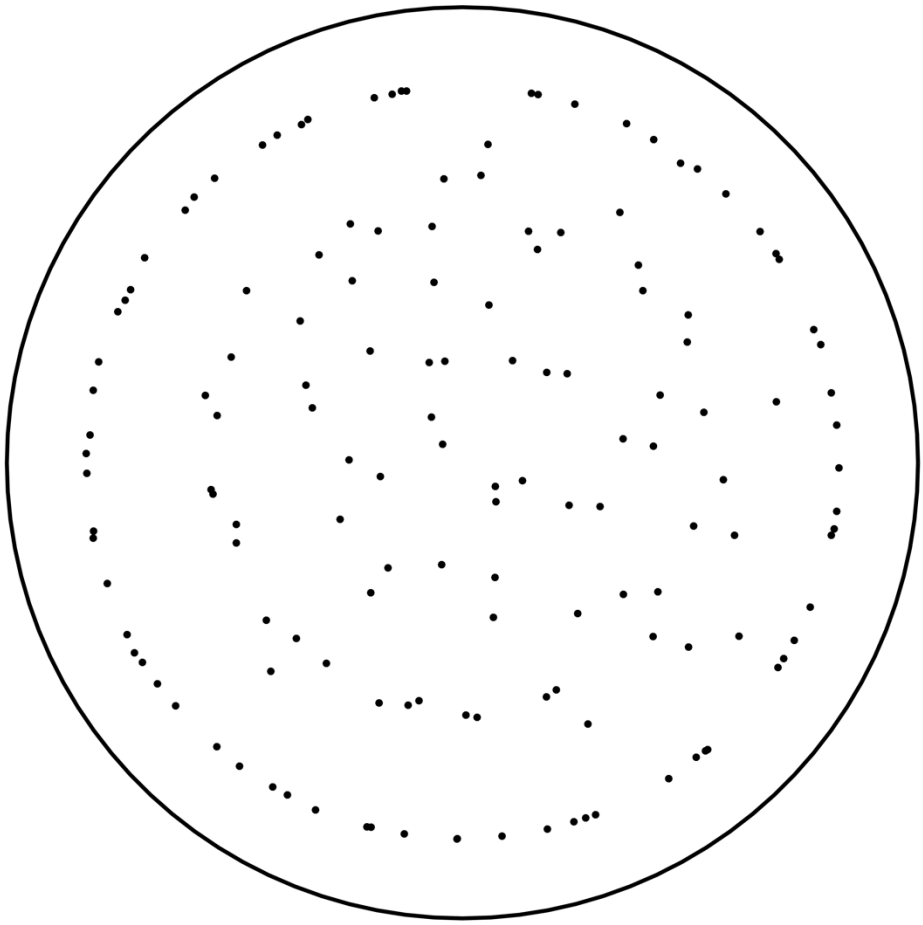

Figure 6: Pebble center locations projected on the cross-section of the bed

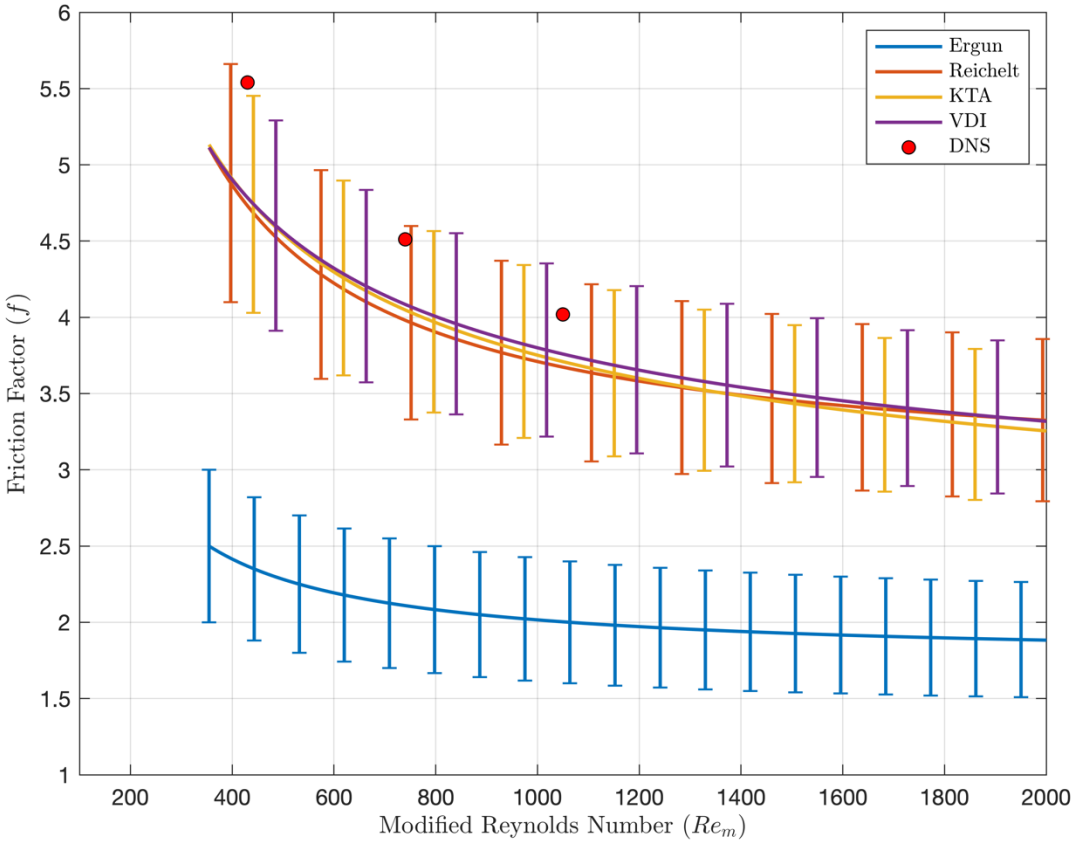


Figure 7: Calculated friction factors at different Reynolds numbers

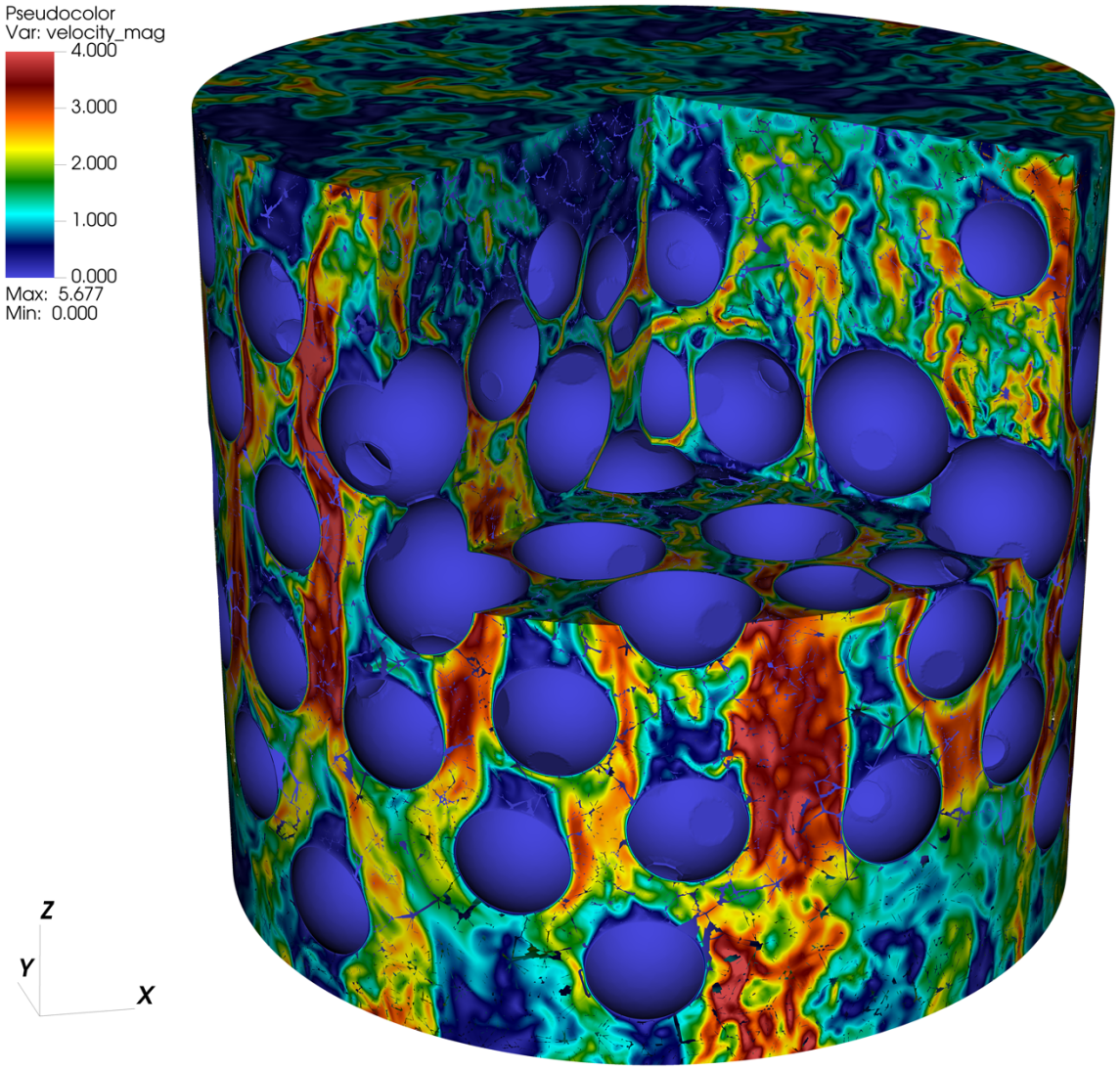


Figure 8: Instantaneous velocity snapshot

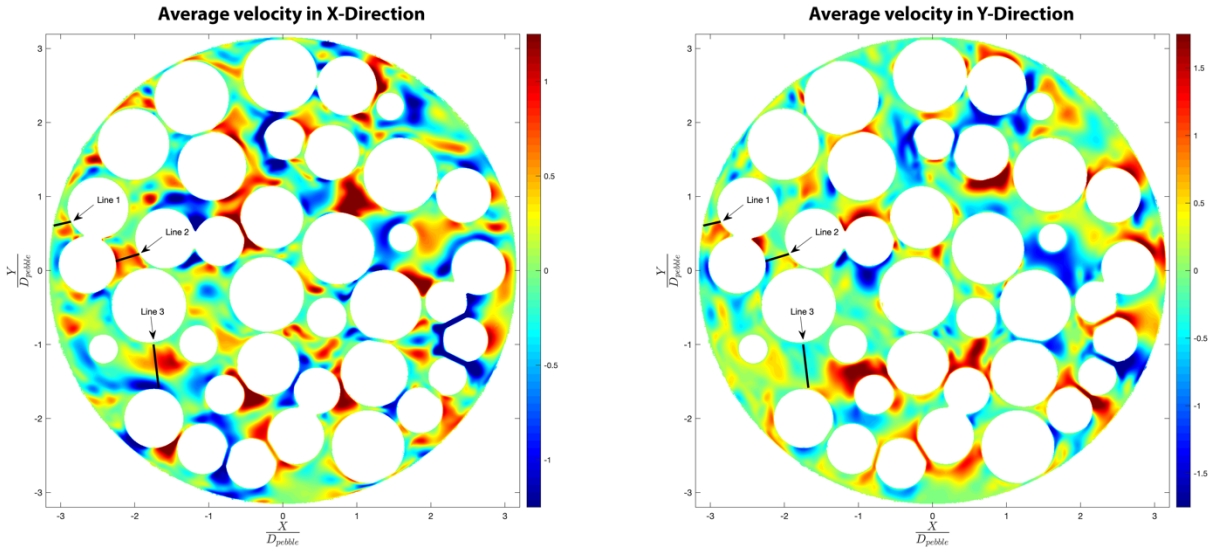


Figure 9: Average velocity profiles with comparison lines

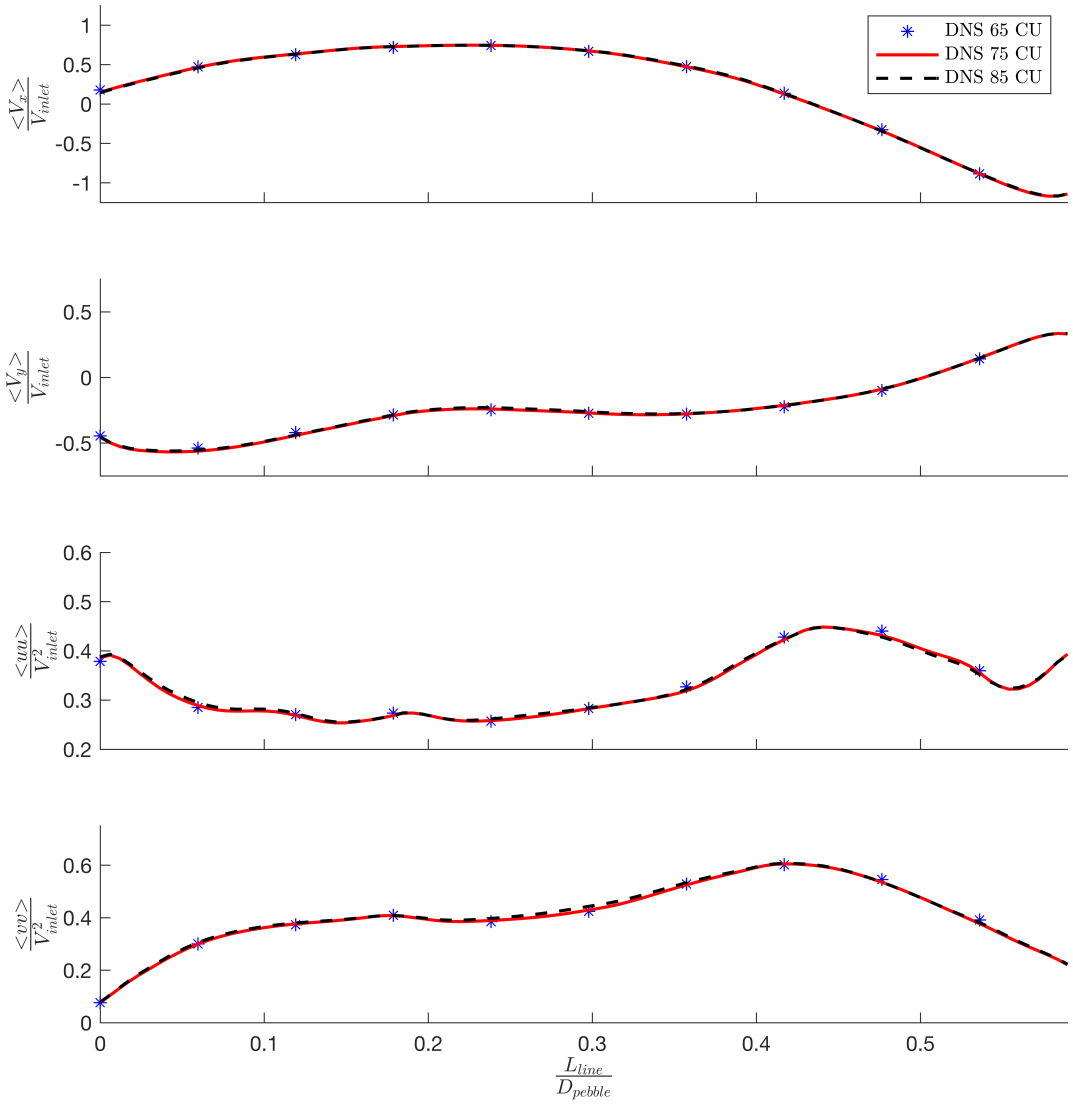


Figure 10: Time convergence of velocity and Reynolds stress components

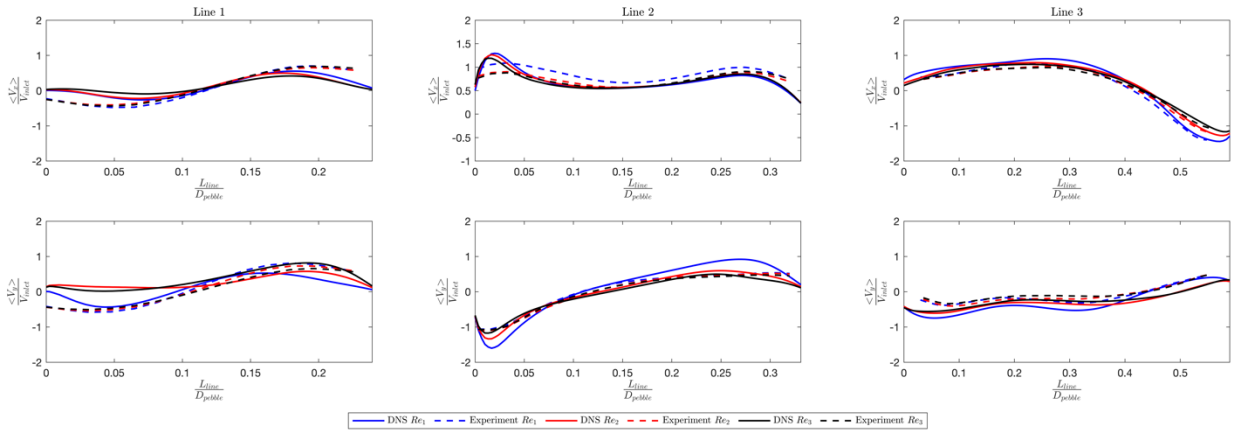


Figure 11: Normalized average velocity profiles (1st row in x-direction, 2nd row in y-direction) for 3 lines

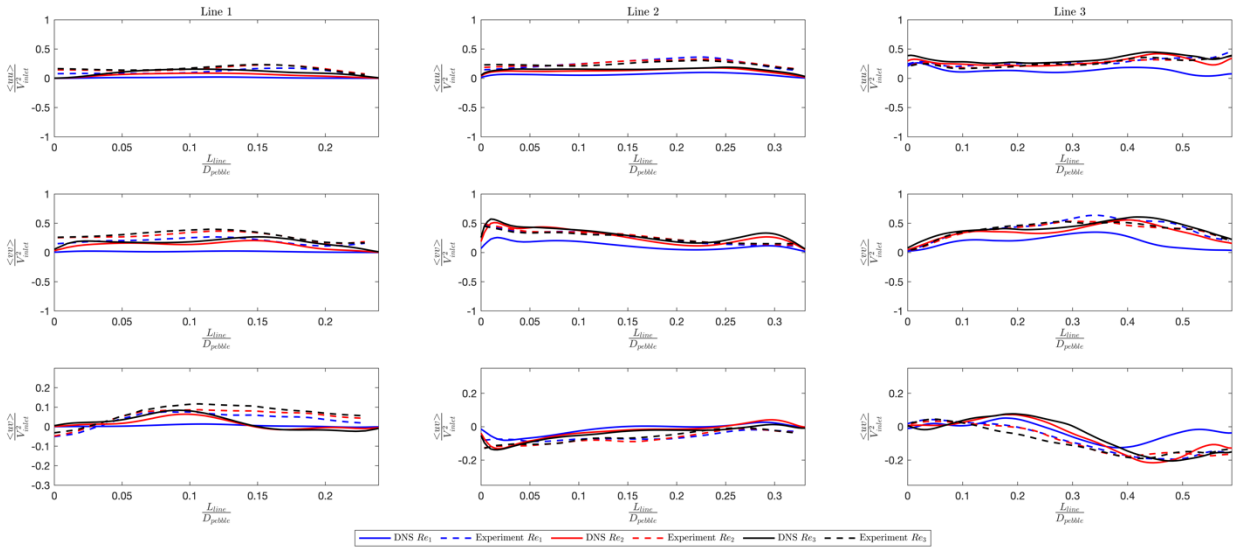


Figure 12: Normalized average Reynolds stresses (1st row – normal stresses in x-direction, 2nd row – normal stresses in y-direction, 3rd row – shear stress) for 3 lines

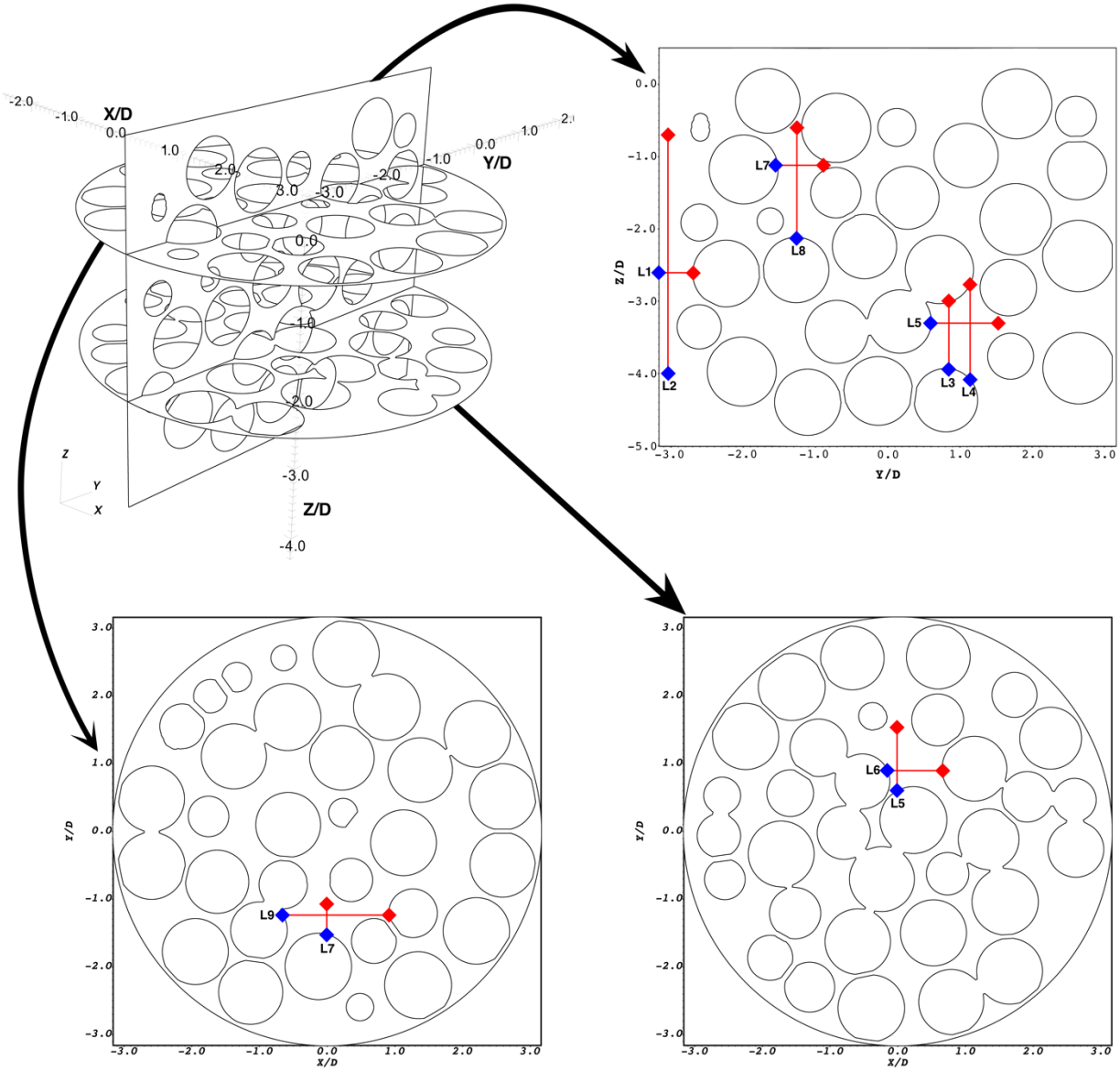


Figure 13: Locations of selected lines for analysis

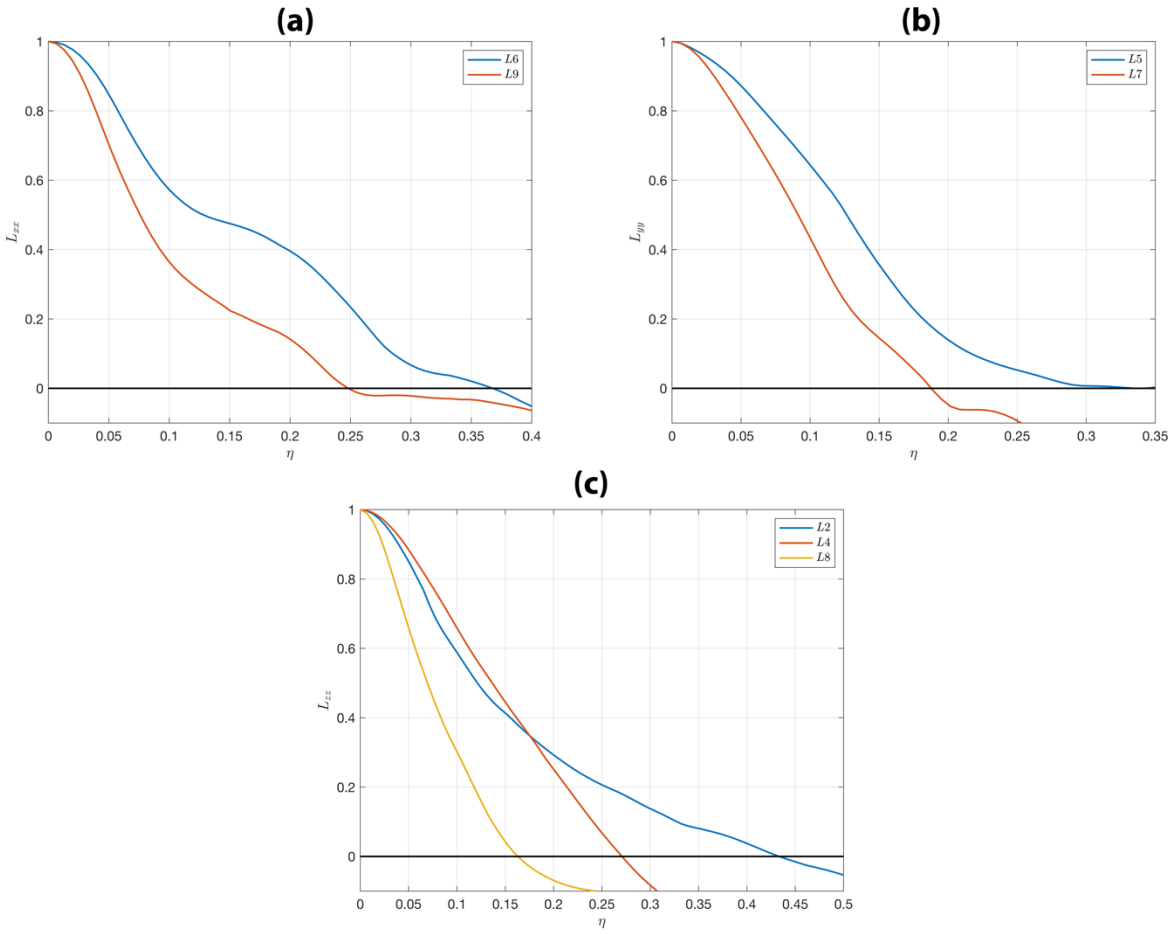


Figure 14: Cross-correlation of velocity fluctuations

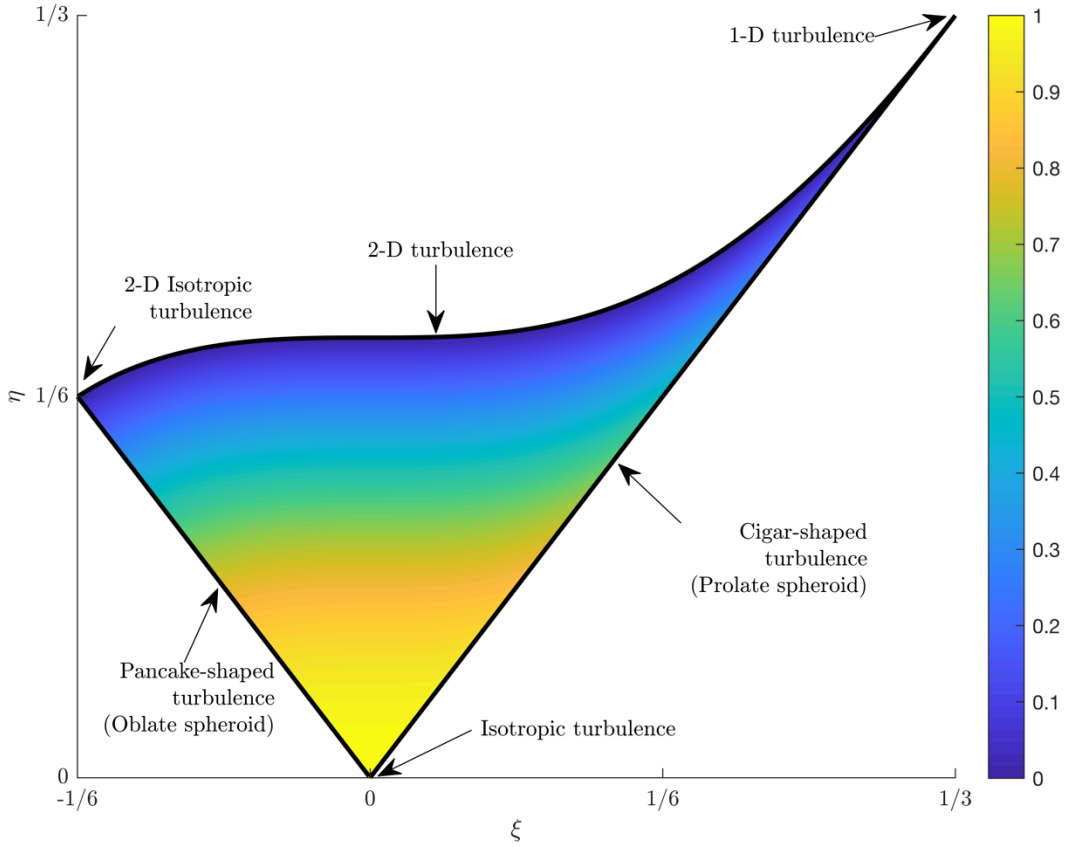


Figure 15: Turbulence triangle showing the limits of the realizable turbulence

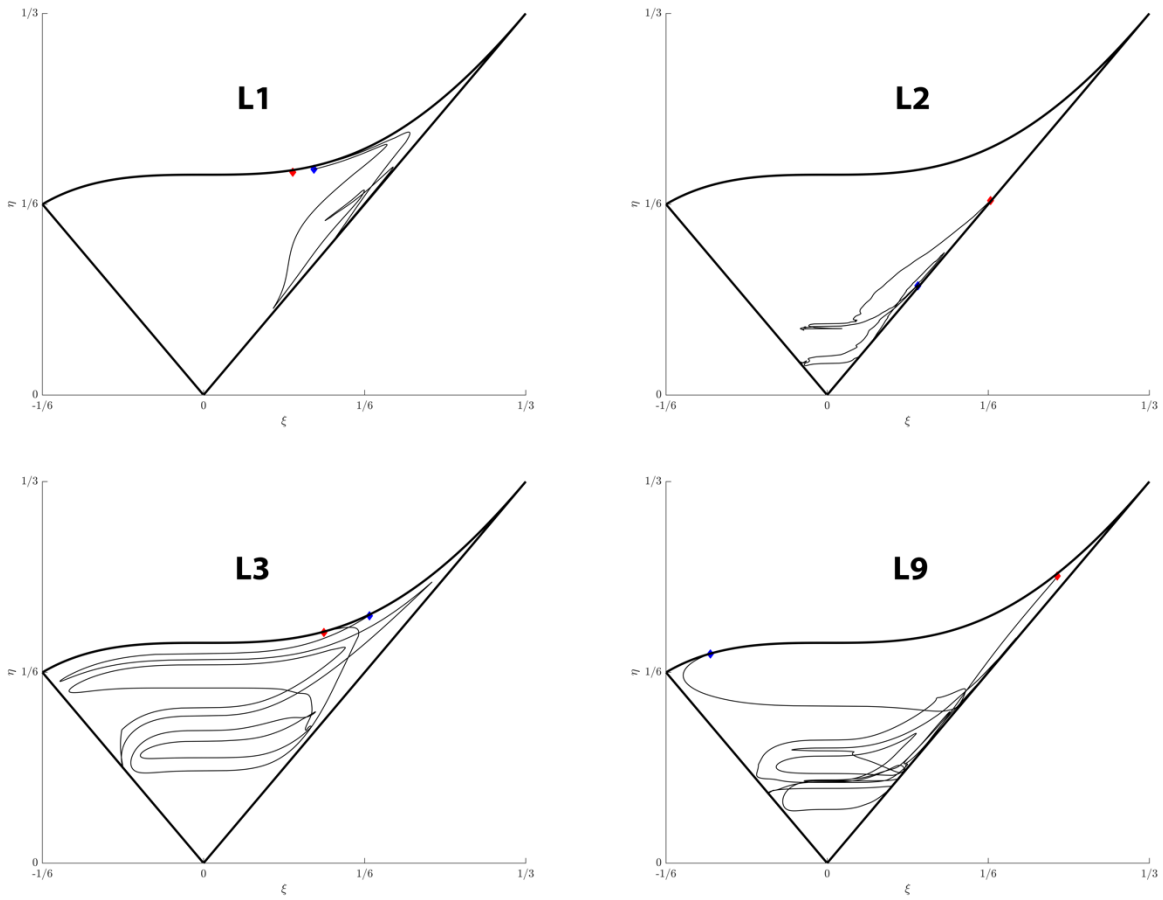


Figure 16: Reynolds stress anisotropy states for selected lines

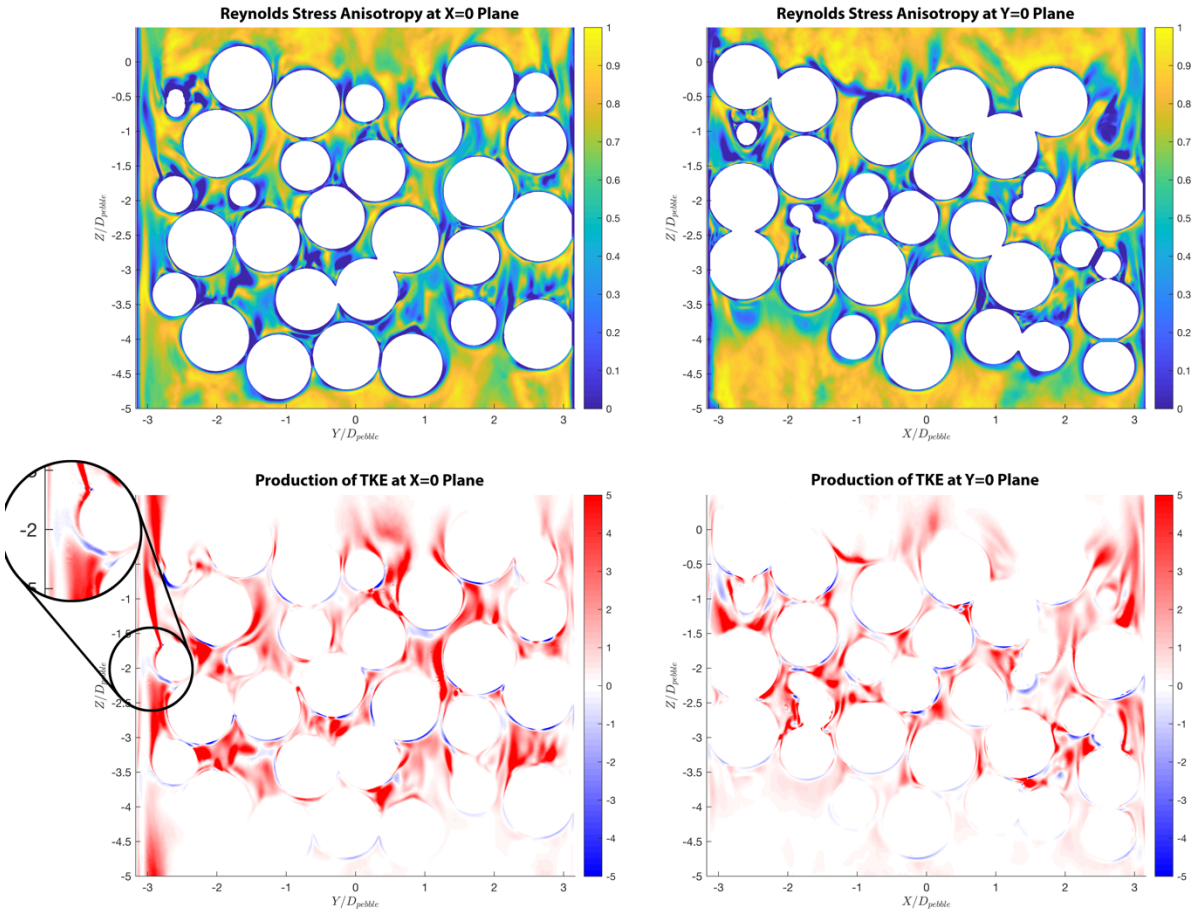


Figure 17: Contours of anisotropy factor (F) X = 0 plane (top left), Y=0 plane (top right) and production of TKE at X = 0 plane (bottom left), Y=0 plane (bottom right)

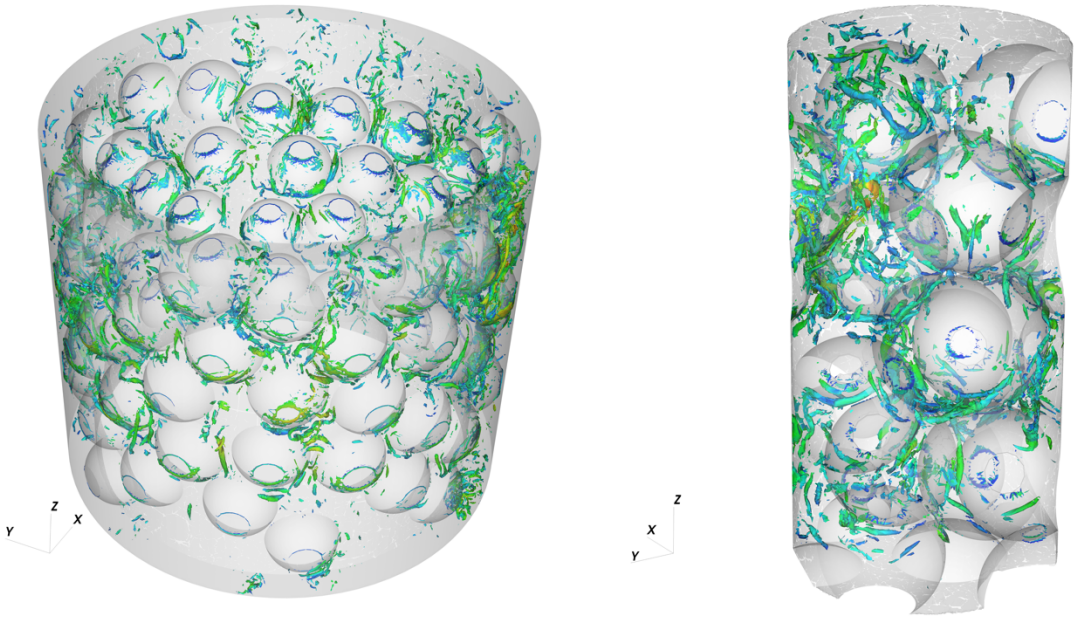


Figure 18: Instantaneous isosurfaces of $\lambda_2$ near the enclosing wall (left) at the center of the bed (right)

# Tables

Table 1: Comparison of bed overall porosity with porosity correlations from literature

| Correlation Name | Evaluated Porosity ($\varepsilon$) | % Difference |
|---|---|---|
| De Klerk [17] | 0.425 | 2.52 |
| Dixon [18] | 0.4184 | 4.06 |
| Jeschar [19] | 0.4291 | 1.61 |

Table 2: Friction factor correlations

| Name | Correlation | Wall Correction |
|---|---|---|
| Ergun | $f = \frac{150}{Re} + 1.75$ | No |
| Eisfeld and Schitzlein | $f = \frac{154\left(1 + \frac{2}{3(D/D_{pebble})(1-\varepsilon)}\right)^2}{Re} + \frac{1 + \frac{2}{3(D/D_{pebble})(1-\varepsilon)}}{\left[1.15\left(\frac{D_{pebble}}{D}\right)^2 + 0.87\right]^2}$ | Yes |
| KTA | $f = \frac{320}{Re} + \frac{6}{Re^{0.1}}$ | Yes |
| VDI | $f = \left(\frac{0.4}{\varepsilon}\right)^{0.78}\left(\frac{317}{Re}\right) + \frac{6.17}{Re^{0.1}}$ | Yes |